STEADY AND UNSTEADY SIMULATIONS OF AEROSTABIL WINDTUNNEL EXPERIMENTS

Bernd Stickan[1] **and Johannes Dillinger**[1]

[1]DLR - Institute of Aeroelasticity
Bunsenstraße 10, 37073 Göttingen
Bernd.Stickan@dlr.de
Johannes.Dillinger@dlr.de

Keywords: Aerostabil, CFD-CSM-Interaction, TAU, Nastran, ModGen, Forced Motion

Abstract:

CFD-CSM coupled simulations of the 2001/2002 Aerostabil windtunnel experiments, making use of a beam finite element model and RANS computations have not agreed satisfyingly with the experimental data.
A detailed analysis has led to the generation of a new shell FEM-model which improved the simulations enormously. The new model showed that the deviations can be explained by airfoil deformations of the wing. By using data from the 2011 FLIB experiment the FE-model has been updated and finally is used for the simulation of a complex steady flow setting.

1 INTRODUCTION

In 2001/2002 a series of measurements had been performed on the so-called Aerostabil wing (model B) to develop a thorough understanding of the static and especially the dynamic behavior of an elastic wing under aerodynamic loading close to the flutter speed [1].

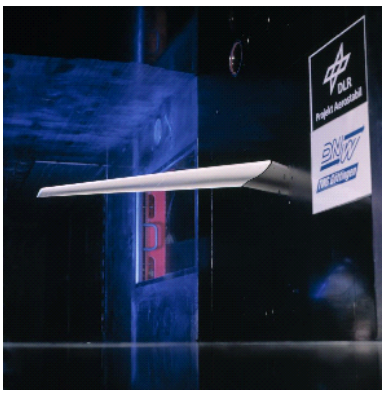

Figure 1: Aerostabil model inside the TWG

The wing model with supercritical airfoils has a span of 0.601m, an aspect ratio of 3.68, a leading-edge sweepback angle of 32°, and is built of glass and carbon fiber composite materials. Measurements have been performed in the Transonic Windtunnel Göttingen (TWG) with *Mach*-numbers ranging from 0.5 to 0.89 and *Reynolds*-numbers from $0.7e6$ to $2.2e6$. For *Mach*-numbers at about $Ma = 0.87$ and angles of attack around $\alpha = 2.6°$ Limit-Cycle-Oscillations (LCO) could be observed with a 50 Hz frequency. Fig. 2 shows the basic equipment of the wing with pressure measurement devices.

Steady *Reynolds*-averaged Navier-Stokes (RANS) computations including fluid-structure coupling to a beam finite element model (FE-model) revealed large deviations for higher *Mach*-numbers compared to the pressure distributions measured in the experiment. By systematically discarding possible error sources in the aerodynamic calculations, the cause for the deviations could be narrowed down to the restricted capabilities of the beam FE-model.

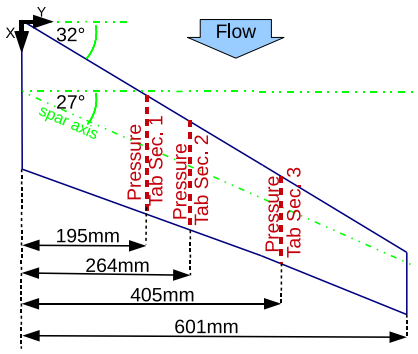

Figure 2: Aerostabil wing sketch:

3 pressure tab sections
upper side: 18/18/15 kulites
lower side: 16/14/12 kulites

leading edge sweepback angle: 32°
spar sweepback angle: 27°

After introducing the numerical methods for computational fluid dynamics (CFD) and computational structure mechanics (CSM), along with a description of the coupling routines in Sect. 2, Sect. 3 describes the generation and adjustments of the first version of the new shell FE-model (SM-V1) of the Aerostabil wing. Sect. 4 introduces shortly the basic aerodynamic models and Sect. 5 finally shows a comparison of simulation results of beam and a first version shell FE-model. Afterwards results of unsteady computations for a CFD-CSM coupled case with strucural excitation or with a classical forced motion method without structural coupling are presented.

In 2011 the FLIB experiment, which included the Aerostabil model as a passive wing to observe gust loads, provivided the opportunity to update and validate the structural model by deformation measurement data. Sect. 6 expains how the model was updated, resulting in the second version of the structural model (SM-V2), along with simulation results of the steady part of the FLIB experiment for the updated second FE-model. In Sect. 7 the results for a complex flow setting close to the LCO with *Mach*-number $Ma = 0.86$ and an angle of attack of $\alpha = 2.6°$ are presented, using SM-V2.

2 NUMERICAL METHODS

The steady and unsteady simulations are performed by stepwise computation loops containing a CFD-solver, a CFD-mesh deformation tool and either a "weak coupled" structural solver (2.a) or a forced motion method (2.b), which applies a complex input mode to the aerodynamic surface. These methods are integrated into the *FlowSimulator* simulation environment [2]. It allows in-memory data exchange between different modules instead of slowing down the process by file input/output.

The included methods in more detail:

1. **CFD Solver - DLR TAU Code**
   The *DLR TAU Code* is a finite-volume solver for the *Reynolds-Averaged Navier-Stokes* (RANS) or *Euler* equations on unstructured grids [3].
   For the RANS computation results the Menter SST turbulence model [4] and as spatial discretization a central scheme with implicit Backward-Euler relaxation and scalar dissipation is used. Dynamic computations are performed with a dual time-stepping method with second-order accurate backward differencing.
2. (a) **CFD-CSM Coupling Method**
   The coupling of structural and aerodynamic surface is done by the interpolation matrix H which is generated with radial basis functions. The matrix H is used

to interpolate the structural deflections u_s to the aerodynamic nodes to get their deflection u_a by

$$u_a = H u_s. \tag{1}$$

Furthermore the aerodynamic forces f_a are transferred to the structural surface using the identical interpolation matrix to get the structural loads f_s by

$$f_s = H^T f_s. \tag{2}$$

This approach guarantees global energy conservation. For more detailed information it is referred to [5].

Structural Solvers

Two different structural solvers have been used for the computation of the structural deflections. Either a modal solver or a solution computed directly by the finite element code *Nastran*.

- **Modal Solver**
  This method uses a modal approach to solve the equilibrium of forces equation in the generalised form:

  $$\Omega q = \Phi_s^T f_s, \tag{3}$$

  where Ω are the structural eigenvalues, Φ_s the structural eigenmodes. The deflections of the structural surface grid can be computed by $u_s = \Phi_s q$. This approach has also been used for CFD-CSM coupled unsteady simulations. To do so equation 3 is expanded by the time variant part $\ddot{q}$ of the generalised coordinates while the inertia part is neglected. This leads to

  $$\ddot{q} + \Omega q = \Phi_a^T f_a. \tag{4}$$

  For the temporal coupling a "Conventional Serial Staggered" algorithm with a predictor-corrector step for the structural displacements is used during the unsteady simulations. Further information can be found in [6].
- **Nastran**
  The commercial finite element solver *MSC Nastran* ([7]) is an analysis tool for the computation of a large variety of structures. In the present paper only the linear static solution is used which solves the equation

  $$K u_s = f_s, \tag{5}$$

  where K is the structural stiffness matrix.

.

(b) **Forced Motion Method**

For the computation of unsteady aerodynamic forces without CFD-CSM coupling a forced motion method is applied. Therefore a complex input mode M,

$$M_k = \mathrm{Re}\left(M_k\right) + i \cdot \mathrm{Im}\left(M_k\right) = \mathrm{Mag}\left(M_k\right) \cdot \exp\left(i \cdot \mathrm{Angle}\left(M_k\right)\right), k \in [1, na], \tag{6}$$

is applied harmonically to the steady deformed surface coming from a CFD-CSM simulation by adding

$$u_k\left(t\right) = \mathrm{Mag}\left(M_s\right) \cdot sin\left(\omega t + \mathrm{Angle}\left(M_k\right)\right), k \in [1, na] \tag{7}$$

to all surface points $k \in [1, na]$. The angular frequency ω is therefore defined with the applied reduced frequency $f^* = 2\pi f c_{ref}/u_\infty$ by

$$\omega = \frac{f^* c_{ref}}{u_\infty}, \tag{8}$$

where c_{ref} is the mean chord length as reference length and u_∞ the reference volcity.

3. **CFD-Mesh Deformation**
   The mesh deformation module uses scattered data interpolation with radial basis functions to transport arbitrary surface deformations into the volume mesh. It is very robust and due to advanced base point selection methods the quality of the deformed grid is very good. Furthermore a "nearest neighbour correction"-step avoids interpolation errors of the CFD surface mesh. The general deformation approach can be found in [8].

3 STRUCTURAL MODEL

The reduced structural representation of an aircraft wing as a beam is typically a well-approved and frequently used method to perform static or dynamic deformation calculations. Important assumptions arising from *Bernoulli* beam theory have to be met when applying *Nastran* beam finite elements:

- preservation of cross-sectional shape
- shear rigidity
- slenderness of the structure that is to be approximated

Due to the large aspect ratio of the Aerostabil wing, the latter assumption is fulfilled. On the other hand, the wing is build without chordwise ribs, supporting the cross-sectional shape [9]. Therefore the assumption of preservation of cross-sectional shape cannot be ensured.

In order to review the structural behavior with respect to cross-sectional deformations under aerodynamic loading, a shell model was created with an in-house parameterised FE-model generator (*ModGen*), Sect. 3.1. In Sect. 3.2, the derivation of the modal basis, as required by the coupling methods, is depicted.

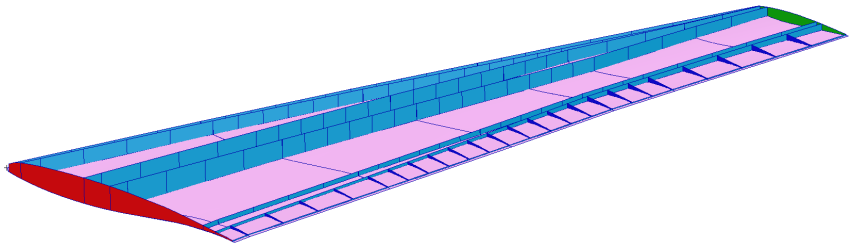

Figure 3: Parameterised geometry

3.1 Model Generation with *ModGen*

ModGen [10], is a parameterised *Nastran* FE-model generator for wing-like structures that successively builds up a geometry model of the main structural components and the

aerodynamic shape, a finite element mesh, an aero model (DLM), an optimisation model, and interface models adopting the connection to other structural entities or non-structural masses like engines and fuel. For the present study, only the finite element mesh will be of interest. The card based text input defines airfoil shapes, wing planform, and the position of structural entities like skins and spars. Along with the meshing parameters, the element properties and material properties conclude the FE-model definition.

Nastran provides basically two ways to model orthotropic material stackings:

- modelling of each single layer by orthotropic material data, layer thickness and fiber angle (`MAT8` / `PCOMP`)
- ABD stiffness representation via membrane, bending, and coupling stiffness matrices (`MAT2` / `PSHELL`)

The methods are equivalent and can be transformed into each other. For Aerostabil, the first method was used.

The basis for the sturctural build-up is a layer scheme that describes the consecutive layers, starting with the outmost carbon and torsion layers and moving inward to the spar and finally web layers. Both, unidirectional layers as well as woven fabrics are used. The latter ones were modelled as two separate layers, accounting for the stiffness loss via a reduction factor of 0.85 (15% dimishment), applied to the theoretical longitudinal stiffness E_1 of a single layer. Unidirectional layer stiffness was adjusted by a reduction factor of 0.95, hence 5% dimishment compared to the theoretical value.

Fig. 3 shows the geometry model of the Aerostabil wing with the top skin removed, as resulting from *ModGen*. In order to simulate a gluing area at the acute trailing edge, dummy ribs were introduced to connect upper and lower skin in the rear area. Arising from the topogical definition within *ModGen*, chordwise and spanwise changes in the layup scheme can be implemented by means of dummy spars and ribs in the geometry model. If not present as real structural entities in the wing, they can subsequently be skipped in the derivation of the FE-model. Part of the spars shown in Fig. 3 are dummy spars.

Structural mass was accounted for by material density definitions for each layup material. Non-structural masses like pressure sensors, accelerometers and wiring were modelled in their center of gravity as point-masses and attached to the load carrying spar construction with interpolating constraint elements (`RBE3`).

3.2 Boundary Conditions and Eigenmodes

The Aerostabil model is clamped at the wing root with the help of a plane bracket, extending from $x \approx 2.0 - 18.5$ cm, measured from the nose. To realistically simulate the wing clamping condition in the FE-model, a rigid body element was applied (`RBE2`), gathering the bracketed part into a single grid point. The finite stiffness of the real clamping was accounted for by torsion springs in the clamping grid point. The coordinate system for the torsion springs was aligned with the spar and the global z-direction (pointing up). To account for the fact that a modal approach would be used for the aeroelastic computations, the torsion spring stiffnesses were adjusted in order to yield a good agreement with the measured frequencies and eigenformes in [1].

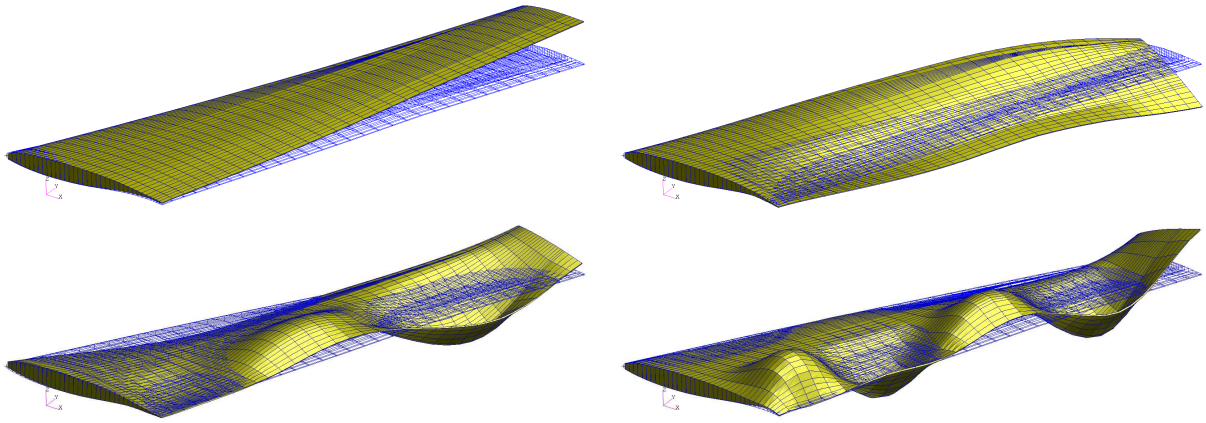

Figure 4: Mode 1, 4, 7, 11 (left to right, top to bottom)

Fig. 4 exemplarily shows modes 1 (1. bending, 37.81 Hz), 4 (1. torsion, 263.43 Hz), 7 (449.03 Hz), and 11 (604.10 Hz). The first bending and first torsion frequency compare very well with the measurements in [1], being 37.81 Hz and 272.60 Hz. Apparently, already for lower modes the cross-sections are not preserved, indicated by a local deformation of the upper and lower wing skins aft of the stiff carbon fiber main spar. This denotes the need for a shell instead of a beam FE-model for the coupled simulations.

4 AERODYNAMIC MODELS

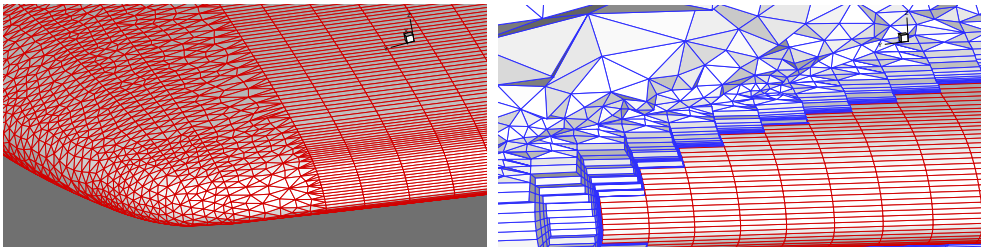

Figure 5: Exemplary CFD model plots: left - surface mesh tip, right - surface mesh and volume mesh extract at leading edge

For the different settings in the following section (Aerostabil alone, Aerostabil plus NACA, Aerostabil plus windtunnel walls) different unstructured CFD meshes have been generated with the Centaur mesh generator [11]. All meshes have mainly hexahedron elements for the discretisation of the wing boundary layers, while the remaining boundary layers are discretised with prism elements. For the remaining volume pyramid- and tetra-elements have been used. The wind-tunnel model has a transition tripping stripe at 7.5% which is also modeled in the CFD-computation. An impression of the grids can be observed in Fig. 5. More details to the different grids are given in each result section.

5 SIMULATION RESULTS FIRST FE-MODEL

5.1 Comparison Beam - Shell Model

In this section two exemplary test cases have been selected to compare the coupled simulation results for the beam and the first version shell FE-model (SM-V1). For this section the structural defelections are computed via the modal approach with 80 eigenmodes.

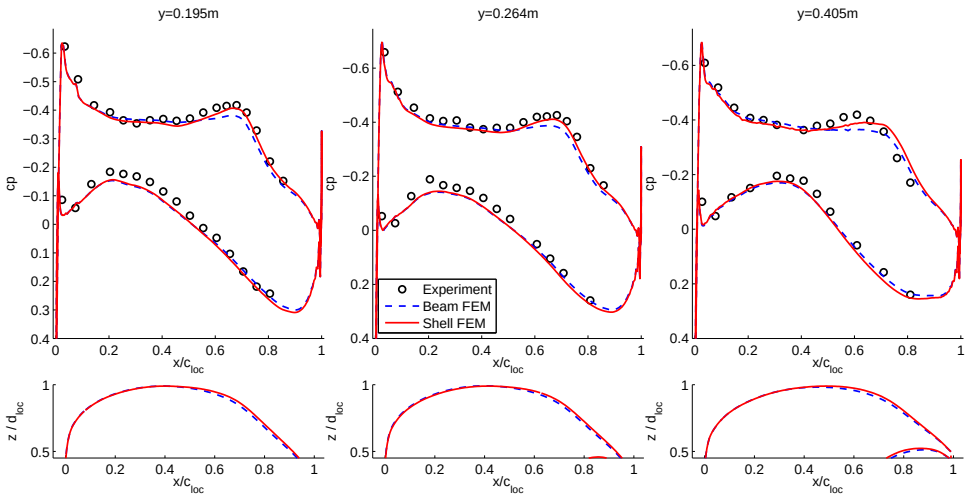

Figure 6: Comparison of beam and shell FE-model results for *Mach*-number $Ma = 0.5$, *Reynolds*-number $Re = 1.2e6$, *Sutherland* constant $Su0 = 0.36$ and angle of attack $\alpha = 0.0°$: Upper plots - pressure coefficient for the 3 measurement sections, lower plots - airfoils of these sections normalized by profile thickness (shifted onto each other for comparison), maximal deformation beam/shell FE-model $dz_{max} = 1.9$ cm/2.0 cm

The CFD mesh comprises 4.5 million nodes and 9.79 million elements. Furthermore the setting contains a viscid wing-side-wall, whose length is fitted to boundary layer thickness measurements from the windtunnel. The opposite side-wall of the 1 m wide TWG uses an Euler boundary condition while the remaining boundaries have farfield conditions.

Fig. 6 shows the comparison for a subsonic test case with *Mach*-number $Ma = 0.5$ and an angle of attack $\alpha = 0.0°$. The difference between beam and shell model is not very large, but the shell model shows slightly improved results for all measurement sections. Furthermore the figure shows the influence on the airfoil shapes at the tab sections. The rear part of the airfoils show little deformation for the shell model while the beam model airfoils naturally remain rigid.

The second, transonic test case has been performed again for $\alpha = 0.0°$, but $Ma = 0.819$. Fig. 7 demonstrates the importance of the advanced structural modelling. The pressure coefficient from experimental data shows on the upper side a large peak which is terminated by a shock. This phenomenon can only by captured by the shell FE-model and can be explained by a local deformation on the upper side of the wing.

The agreement of measured and calculated pressure distributions is less good in the outer section where the mentioned peak is predicted too far aft.

5.2 Unsteady Simulations

The unsteady measurements were conducted for a pitching motion along the spar axis sketched in Fig. 2. The acceleration sensors installed in the model show that the excitation leads to a combination of pitch and bending. Therefore, two different methods have been tested, a forced motion (FM) method combining the first bending mode and the rigid rotational mode, and additionally a CFD-CSM coupled computation with excitation of the structural model by force input (CFDCSM).

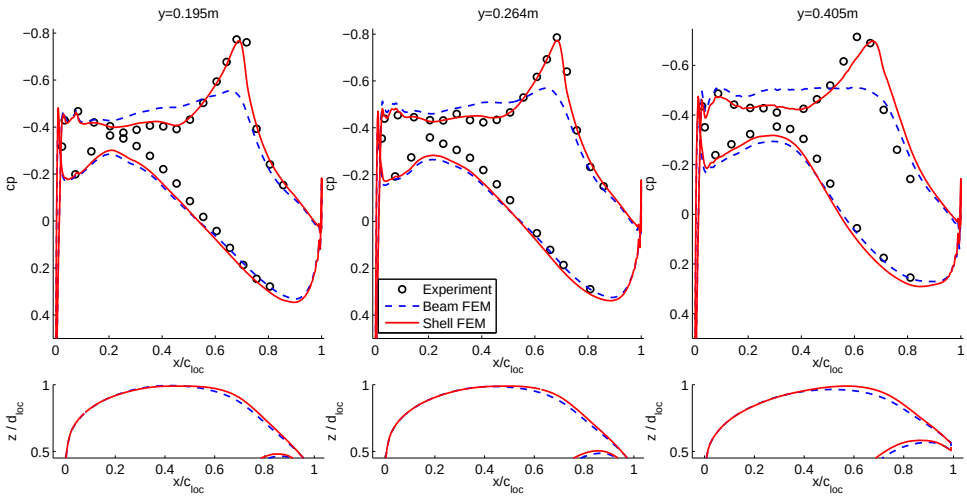

Figure 7: Comparison beam FE-model and shell FE-model (SM-V1) results for *Mach*-number $Ma = 0.819$, *Reynolds*-number $Re = 1.3e6$, *Sutherland*-constant $Su0 = 0.36$ and angle of attack $\alpha = 0.0°$: Upper plots - pressure coefficient for the 3 measurement sections, lower plots - airfoils of these sections normalized by profile thickness (shifted onto each other for comparison),maximal deformation beam/shell FE-model $dz_{max} = 3.15$ cm/3.35 cm

For the coupled method the FE-model has been expanded with pitching arms at the root section as sketched in Fig. 8. This allows to model the windtunnel mechanics without a rotational degree of freedom in the structural equations. The wing has been pitched during the unsteady simulations by applying a harmonic force onto the arms.

The amplitude of the first bending mode for the forced motion method is defined by the integrated signal of an acceleration sensor close to the tip of the wing. Since not all acceleration sensors installed in the model show trustworthy signals, the coupled method should help to assure the assumption of combining bending and rigid pitching.

5.2.1 Comparison of CFD-CSM Coupled - and Forced Motion - Method

For a subsonic flow setting with $Ma = 0.5$ the two introduced methods are compared in terms of the complex first harmonic of the transfer functions $c_{p,\beta}$ with the pitching angle $\beta(t)$ as input and the pressure coefficient c_p as output variable (pressure derivative). Fig. 9 shows for three different reduced frequencies the pressure derivatives for the middle pressure tab section.

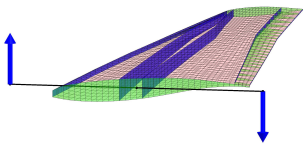

Figure 8: FE-model with attached arm

The two methods show a satisfying agreement, which supports the assumption to use a combination of bending and rigid rotation. The agreement with the experimental data is good in magnitude for all cases, but the phase agreement especially for the high reduced frequency is not adequate. Table 1 presents some details about the complex input mode for the forced motion method. In addition, the maximal deformation of the harmonic surface motion can be analysed by comparing $\max(\mathrm{Mag}(M_{z,FM}))$ and $\max(\Delta z_{CFDCSM})$. It can be recognized that the excitation frequency of the second setting, which is close to the eigenfrequency of the first bending mode, leads to mode excitation. This behaviour can not be identified for the CFD-CSM simulation. For a subsonic flow setting with $Ma = 0.5$ the two introduced methods are compared in terms of unsteady

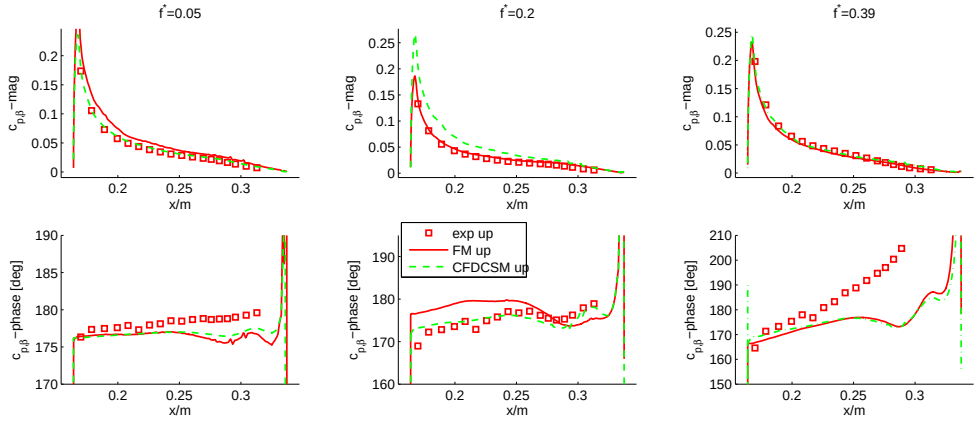

Figure 9: Comparison of first harmonic pressure derivative results $c_{p,\beta}$ from forced motion method (FM) and CFD-CSM coupled method with external pitching force excitation (CFDCSM) for the upper side of the $y = 0.264m$ pressure tab section and different reduced frequencies f^*, flow settings: $Ma = 0.5$, $Re = 1.22e6$, $S.u0 = 0.36$, $\alpha_{simulation} = 0.09°$, CFD-solver: Euler

f^*	$\Delta\beta[deg]$	$\Delta\phi_{bending}[deg]$	$\max(\mathrm{Mag}(M_{z,FM}))\,[mm]$	$\max(\Delta z_{CFDCSM})\,[mm]$
0.05	0.256	0.0	0.54	0.927
0.2	0.269	19.0	1.9	0.926
0.39	0.301	174.0	1.04	0.948

Table 1: Forced motion method settings for $Ma = 0.5$: $\Delta\beta$ - pitching angle amplitude, $\Delta\phi_{bending}$ - phase difference between rigid rotation and first bending mode, $\max(\mathrm{Mag}(M_{z,FM}))$ - maximal mode displacement in z-direction, $\max(\Delta z_{CFDCSM})$ - maximal displacement in z-direction of corresponding CFDCSM computation

aerodynamic pressures. Figure 9 shows for three different reduced frequencies the pressure derivatives for the middle pressure tab section.

5.2.2 Forced Motion Results for Transonic Flow Setting

Since the previous section has shown that the combination of rigid rotation and first bending mode with an amplitude defined by the integrated acceleration signals of an outer sensor leads to satisfying results, this method has been applied to three transonic test cases with $Ma = 0.819$ and $Re = 1.3e6$. The angle of attack α for the computations has been fitted to the mean unsteady pressure coefficients from the experiment, $\alpha_{Simulation} = 0.4°$. Fig. 10 shows acceptable results for the two lower reduced frequencies in terms of $c_{p,\beta}$-amplitude, combined with an unsatisfying phase-agreement. For the high reduced frequency $f^* = 0.3$ the phase of $c_{p,\beta}$ is much closer to the experimental data while the amplitude is too low. Therefore, further investigations into the excited complex form will be necessary.

6 STRUCTURAL MODEL UPDATING AND VERIFICATION

In 2011 the Aerostabil model B was used again for the gust response experiment FLIB, performed in the Transonic Windtunnel Göttingen. The experimental setup consisted of a 2D NACA 0010 wing, acting as gust generator, and further downstream - passively mounted to the windtunnel wall - the Aerostabil wing. The CFD-mesh in Fig. 14 illustrates this setup. The NACA wing has a root chord length of 0.3 m and the distance between NACA leading edge and Aerostabil root leading edge is 1.127 m. [6]

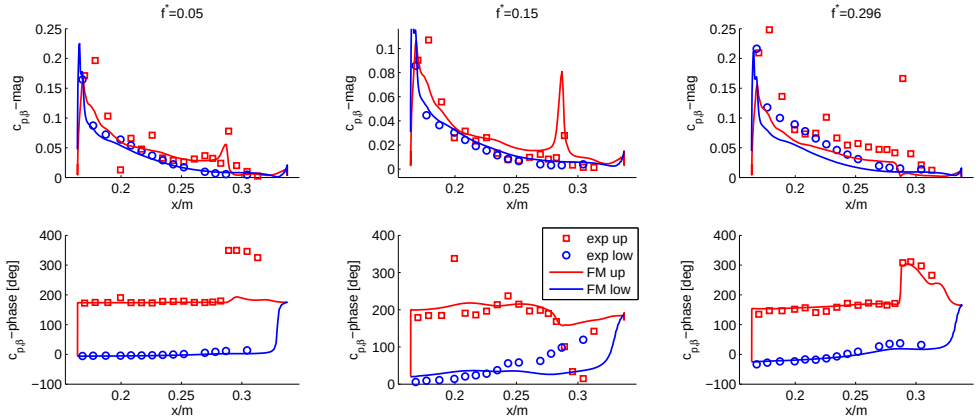

Figure 10: First harmonic pressure derivative results $c_{p,\beta}$ from forced motion method for the $y = 0.264m$ pressure tab section and different reduced frequencies f^*, flow settings: $Ma = 0.819$, $Re = 1.3e6$, $Su0 = 0.36$, $\alpha_{simulation} = 0.4°$, CFD-solver: RANS

To determine local deflections of the Aerostabil wing as a result of aerodynamic and gust loads invoked by the gust generator, a marker-based deformation measurement system was applied.

Among measurements with a flipping gust generator wing, also measurements with a non-moving gust generator ($\alpha_{NACA} = 0°$) were performed. Furthermore, the installation was used to conduct static wind-off measurements by applying weight forces at a defined position in the wing tip region and measuring the static deflection at the marker-positions. This second set of steady wind-on and static wind-off measurements (aside from the first measurement set [1]) offered the opportunity to improve the FE-model and validate results of the coupled CFD-CSM simulations.

6.1 Structural Model Update

As mentioned, a set of markers was used to measure the static and dynamic deflection of the Aerostabil wing. The distribution of markers is shown in Fig. 6.1, along with the force application position for the static wind-off test. The markers are applied in 6 $y = const.$-cuts at leading and trailing edge, as well as inbetween for cut stations 3 and 4.

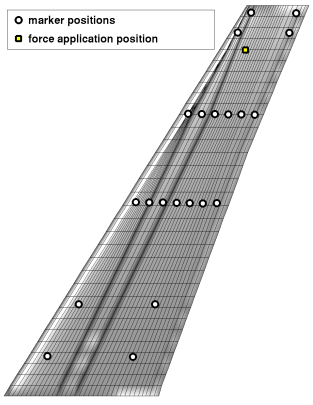

Figure 11: Marker and force application positions

For the static test, the wing was loaded by means of weight plates up to a maximum of 7.668 kg. The same test was modelled in the FE-calculations, subsequently comparing the deflections at marker positions. For this purpose the FE-grid the closest to each marker position was picked for the following comparison plots.

Fig. 12 presents the static deflection results of the initial shell model (SM-V1) as described in Chap. 3, compared to the experimental data for maximum loading of 7.668 kg. The upper plot shows the z-deflection of the frontal (leading edge) markers and the lower plot the z-deflection of the rear (trailing edge) markers, as a function of spanwise position y.

Several changes as described below were introduced in the new shell model version SM-V2.

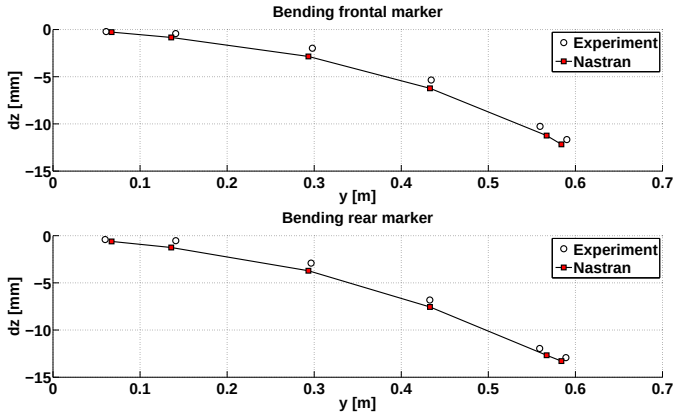

Figure 12: Initial shell model, static deflection comparison

1. In order to better cover the root section stiffness, a steel stick that protruded ≈ 8 cm into the wing inbetween the carbon fiber spar caps in the real Aerostabil wing, was modelled with beam elements and rigidly attached to the spar cross-sections.
2. To increase the FE-model quality, instead of attaching non-structural point masses to the spars, they were rigidly attached to the closest FE-grid in the wing skin.
3. To closer reproduce the experimental static wing deflection shown in Fig. 12, the theoretical longitudinal stiffnesses E_1 of unidirectional layers and woven fabrics were reduced by another 10%, resulting in reduction factors of 0.85 and 0.75 respectively.
4. The trailing edge gluing area was modified to yield a nearly constant glue height at the upstream end.
5. Integration of small corrections to layup angles in the shear core windings.

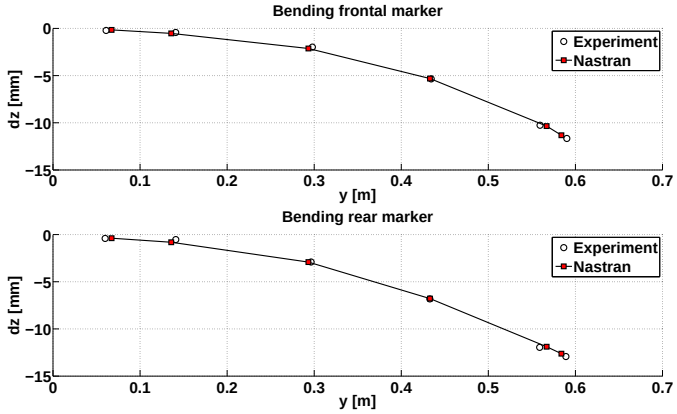

Figure 13: Updated shell model, static deflection comparison

Finally, the torsion spring stiffnesses at the root clamping were adjusted to provide a good agreement with the experimental data, Fig. 13. This is an important difference compared to the first shell model, for which the clamping stiffness was adjusted with respect to measured eigenfrequencies and eigenmodes. The reason for this approach is twofold. As a result of the modified mass attachment the eigenmodes have an even more local character. Hence, the derivation of non-local eigenmodes and their comparison to measured results becomes ambiguous. Only the first and second bending mode can clearly be identified with eigenfrequencies of 40.35 Hz and 117.79 Hz, comparing to 37.81 Hz and 112.85 Hz from measurements [1]. The second reason is based on the fact that the static

measurements are the most updated and accurate results, best representing the wings current condition.

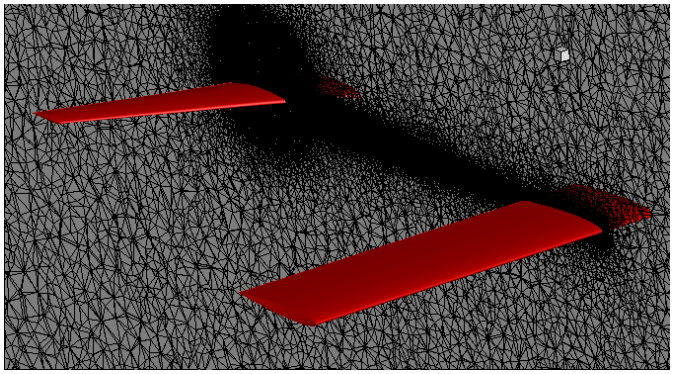

Figure 14: CFD-mesh setting plus volume cut at $y = 0.15$ m for the steady FLIB simulations

6.2 Steady FLIB Simulation Results

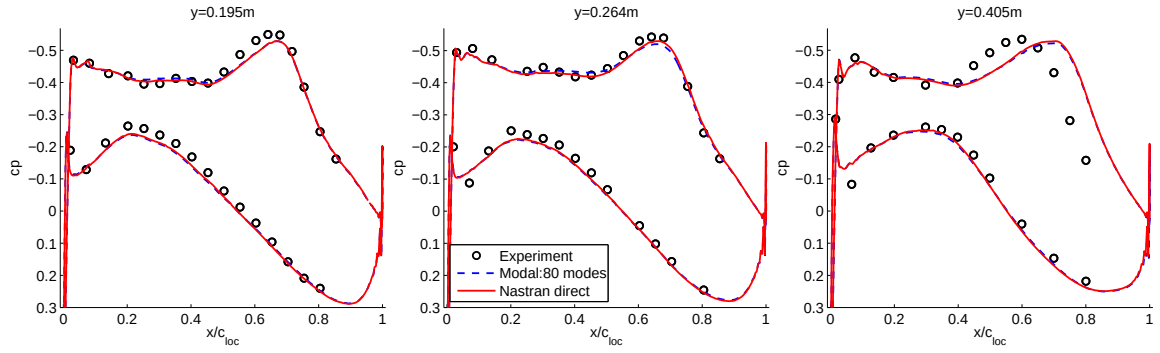

Figure 15: Pressure coefficient results for steady FLIB experiment, *Mach*-number $Ma = 0.75$, *Reynolds*-number $Re = 1.38e6$, *Sutherland* constant $Su0 = 0.36$ and angle of attack $\alpha = -0.1°$

For the simulation a CFD grid with approx. 7 million nodes has been created. The volume mesh between NACA and Aerostabil contains a structural hexahedron block to prevent the NACA wake from dissipating too much. Like in Sect. 5, the windtunnel side wall the Aerostabil is attached to, is modelled as viscid while the opposite wall uses an Euler boundary condition. A volumetric cut of the mesh can be seen in Fig. 14.

In this section the results for a NACA angle of attack $\alpha_{NACA} = 0°$ and an Aerostabil angle of attack of $\alpha = -0.1°$, which is corrected by $d\alpha = 0.3°$ for the computation, is presented.

The *Mach* number is $Ma = 0.75$ and the *Reynolds* number $Re = 1.38e6$ referred to the Aerostabil mean chord length $c_{ref} = 0.183m$. The modal approach and the direct linear *Nastran* solution are used for the structural computation, both coupled to aerodynamics with an identical coupling matrix H.

Fig. 15 shows the pressure coefficient results of the simulations for the two structural simulation method applied. The bending curve along the spar axis and the local angle of attack α_{loc} can be observed in Fig. 16. Clearly, the bending and torsion show a very good agreement compared to the experiment, but the pressure coefficients reveal a deviation in the outer measurement section, for which the peak is too far aft and hence, the loading

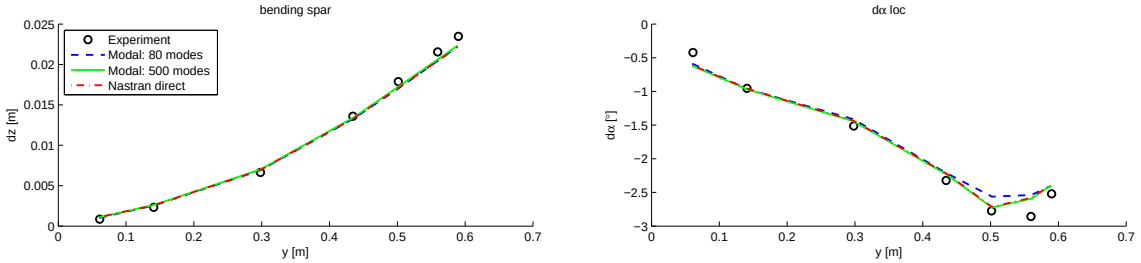

Figure 16: Bending and local change in the angle of attack $d\alpha$: simulation results evaluated by corresponding fictive, linearly interpolated markers

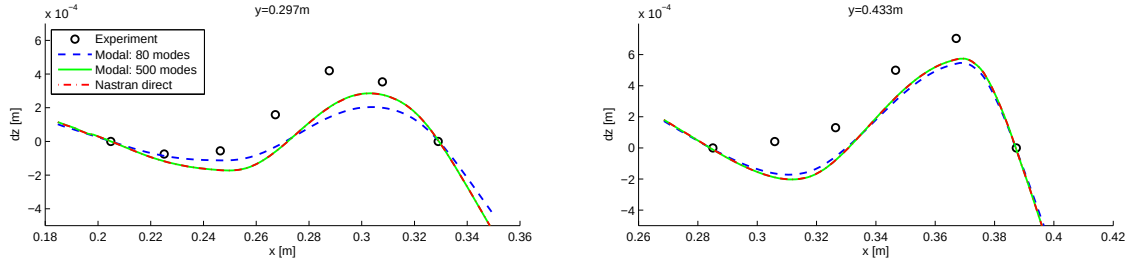

Figure 17: Airfoil deformation dz: First and last measured point in each cut used as $dz = 0$ - reference to compare experiment and simulation

is too high. The good agreement in terms of torsion could lead to the assumption that this load deviation is less large closer to the tip. This assumption is supported by the fact, that the negative peak of the pressure distributions for the two inner measurement section is at 70% chord length and for the last section at about 60% percent, while the simulation results have their peaks for all cuts at 70% percent. Therefore a local structural irregularity close to the outer section could be assumed.

Fig. 17 shows the local deformations for the direct *Nastran*-coupling, but also for the modal approach with different numbers of considered eigenmodes. The plot illustrates that a large number of modes is required in order to get a satisfying agreement with direct coupling method. For a modified SM-V2 version with a larger trailing edge gluing area these differences are even more significant, see Fig. 18.

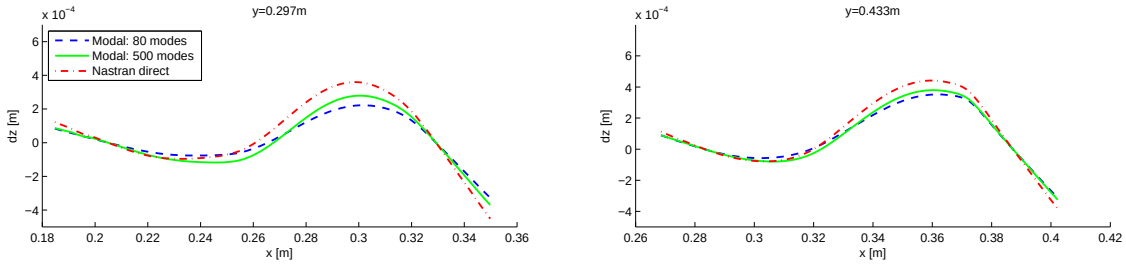

Figure 18: Airfoil deformation dz for modified SM-V2 to show sensitivity of modal approach due to local structural modifications

7 STEADY SIMULATION RESULT FOR LCO-CLOSE SETTING

The most remarkable feature of the 2001/2002 wind-tunnel experiments are the observed Limit-Cycle-Oscillations (LCO) in a certain flow parameter range. In this section a flow setting close to the LCO should be investigated, using the updated FE-model from Sect. 6.

The flow settings are *Mach*-number $Ma = 0.86$, angle of attack $\alpha = 2.66°$ and *Reynolds*-number $Re = 1.26e6$.

The CFD-mesh used for this flow setting contains viscid wind-tunnel walls at all four sides. The upper and lower wall is adapted according to experimental windtunnel settings.

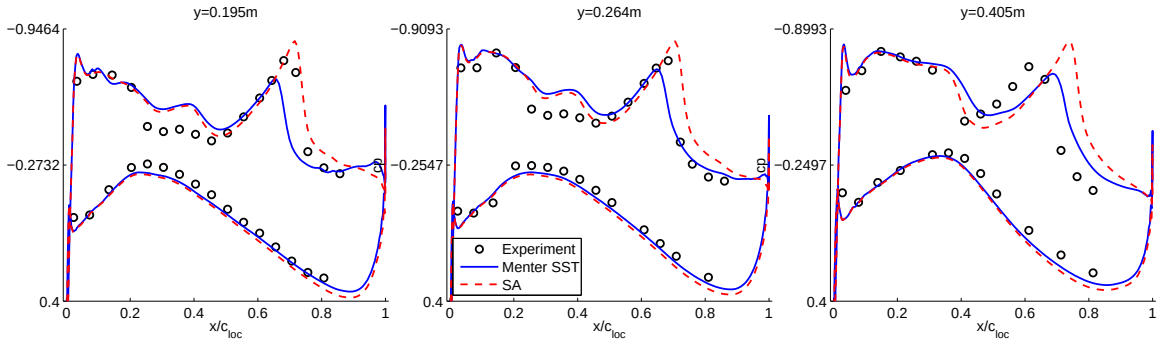

Figure 19: Pressure coefficient results for Menter SST and Spalart-Allmaras (SA) turbulence model, *Mach*-number $Ma = 0.86$, *Reynolds*-number $Re = 1.26e6$, *Sutherland* constant $Su0 = 0.36$ and angle of attack $\alpha = 2.66°$,maximal deformation SST/SAO $dz_{max} = 3.9$ cm/4.1 cm

Fig. 19 shows steady simulation results for the coupling loop using the direct *Nastran* approach on the structural side. For the turbulence modelling not only the Menter SST model is used as in the previous chapters, but also the Spalart-Allmaras model [12]. The larger deviation between measurement and simulation can on the one hand be explained by an unsatisfying FE-model behaviour, but on the other hand Fig. 19 and 20 demonstrate that also the aerodynamic modelling can cause discrepancies. Although the separation areas of both turbulence models show differences in the skin-friction lines, the separation areas behind the shock could give a hint on the mechanism behind the experimental Limit-Cycle-Oscillations.

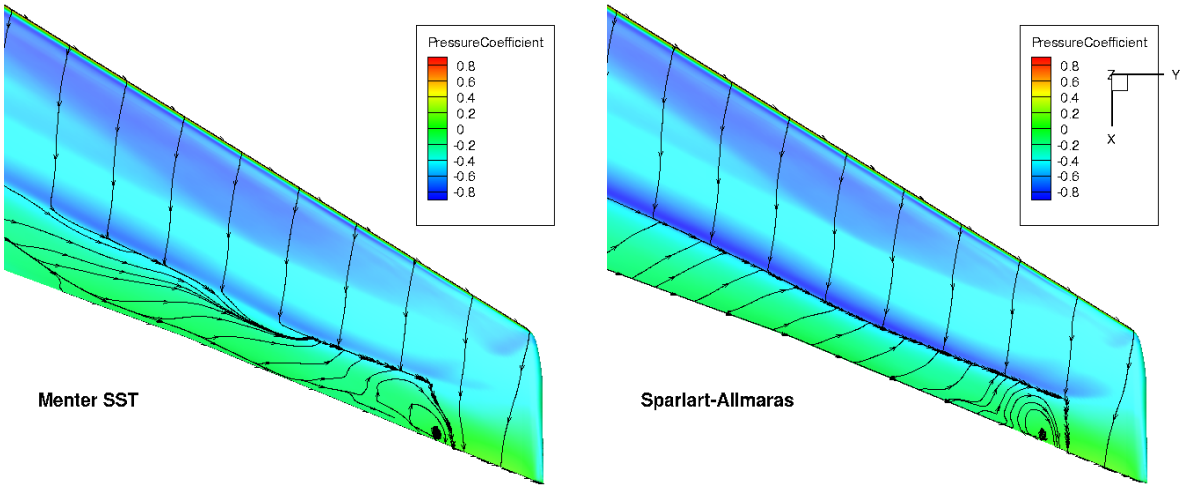

Figure 20: Upper surface skin friction lines and pressure coefficient for Menter SST (left) and Spalart-Allmaras(right) turbulence model

8 CONCLUSION

The investigated Aerostabil experiments have turned out to be a challenging test case for structural modelling and static CFD-CSM coupling methods. The investigated airfoil

deformations have been verified by a new windtunnel experiment and show satisfactory agreement. On the other hand the unsteady forced motion simulation results are not satisfactory and require further investigation. Additionally, the flow setting close to LCO-conditions is very demanding in terms of aerodynamic modelling, but also motivates to refine the structural model further. Uncertainties in structural build-up, meaning possible deviations from the provided layer scheme or in fiber properties, form a large field of investigation. Moreover it is not yet know, which effect material aging and fatigue can have on the structural properties.
Detailed studies will have to be performed in the future in order to clearly separate aerodynamic and structural influences on the calculation results.

9 REFERENCES

[1] Dietz, G., Schewe, G., Kiessling, F., et al. (2003). Limit-cycle-oscillation experiments at a transport aircraft wing model. Proceedings, IFASD 2003, Amsterdam.

[2] Meinel, M. and Einarsson, G. The flowsimulator framework for massively parallel cfd applications. Tech. rep., PARA 2010, Reykjavik.

[3] Kroll, N., Rossow, C.-C., Schwamborn, D., et al. (2002). *Megaflow - a numerical flow simulation tool for transport aircraft design*. Springer (Berlin). ISBN 978-3-540-24383-0.

[4] Menter, F., Kuntz, M., and Langtry, R. (2003). Ten years of industrial experience with the sst turbulence model. Tech. rep., Turbulence, Heat and Mass Transfer 4.

[5] Neumann, J. and Ritter, M. (2009). Steady and unsteady aeroelastic simulations of the hirenasd wind tunnel experiment. Proceedings, IFASD 2009 ,Seattle.

[6] Mai, H., Neumann, J., and Hennings, H. (2011). Gust response: A validation experiment and preliminary numerical simulations. Ifasd paper, IFASD 2011, Paris.

[7] MSC. *MSC-Nastran*. URL: www.mscsoftware.com.

[8] Allen, C. and Rendall, T. (2007). Unified approach to cfd-csd interpolation and mesh motion using radial basis functions. AIAA Paper 2007-3804.

[9] Niu, M. *Airframe Structural Design*. Hong Kong Conmilit Press LTD.

[10] Klimmek, T. (2009). Parameterization of topology and geometry for the multidisciplinary optimization of wing structures. Proceedings, European Air and Space Conference 2009, Manchester.

[11] CentaurSoft. *Centaur*. URL: www.centaursoft.com.

[12] Spalart, P. and Allmaras, S. R. (1992). A one-equation turbulence model for aerodynamic flows. AIAA Paper 92-0439.